Quantum Dynamics Simulations of the Polariton Transport Process

Benjamin X. K. Chng,[†] M. Elious Mondal,[‡] and Pengfei Huo[*,‡]

†*Department of Physics, University of Rochester, Rochester, New York, 14627*
‡*Department of Chemistry, University of Rochester, Rochester, New York, 14627*
¶*Institute of Optics, Hajim School of Engineering and Applied Sciences, University of Rochester, Rochester, New York, 14627*

E-mail: pengfei.huo@rochester.edu

Abstract

Recent experiments have shown that the transport of excitons in organic semiconductors can be significantly enhanced through hybridization with confined photonic modes in a cavity, thereby forming molecular exciton-polaritons (EP). Dissipative mechanisms that affect the constituent states of EPs, such as exciton-phonon coupling and cavity loss, have been observed to diminish their effective velocities in experiments. To elucidate the impacts of these dissipative mechanisms on the transport characteristics of molecular EPs, we develop an efficient quantum dynamics simulation approach that allows us to directly simulate polariton transport dynamics under the collective coupling regime and beyond long-wavelength approximation. Our numerical results suggest a renormalization of the group velocities with stronger exciton-phonon coupling strengths and smaller Q-factor, in agreement with existing polariton transport experiments. Additionally, we observe the transition from ballistic to diffusive EP propagation, as well as the quality factor-dependent behavior of the transient mean square displacement, agreeing well with the recent experimental measurements.

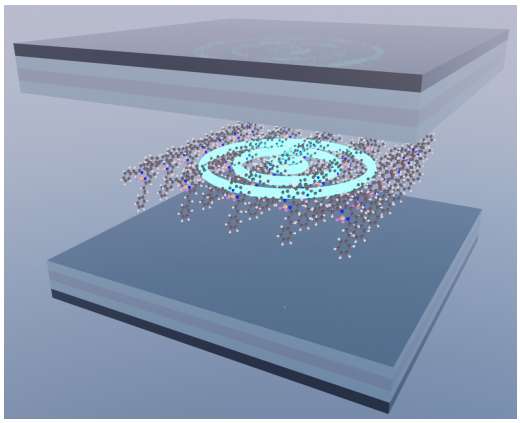

Enabling efficient excitation energy transport is essential for basic energy science and device applications,[1,2] such as organic semiconductors and perovskite structures and light-emitting diode displays.[3–5] However, the inherent disorders and exciton-phonon interactions in these materials restrict the exciton transport, resulting in slow, diffusive motion of exciton, which is often the fundamental bottleneck of the device's performance. For example, investigations of organic molecular semiconductors and halide perovskites have revealed diffusion lengths of around 10 nm[6,7] and 100 nm,[8,9] respectively. The diffusive and short-range exciton transport in these materials imposes significant constraints on their applicability as optoelectronic devices.[10,11]

Recent experiments have demonstrated that exciton transport in organic semiconductors and halide perovskites is significantly enhanced when these materials are strongly coupled to the photonic modes of a cavity.[12–16] This leads to a large group velocity up to 40 μm ps^{-1} for a halide perovskite in a Fabry-Pérot (FP) cavity[14] and up to 180 μm ps^{-1} for an organic semiconductor in a photonic crystal cavity[12] and a micrometer range of transport. The observed fast propagation velocities, which exceed those in the bare material by several orders of magnitude, are due to the formation of molecular polaritons.[17–20] These molecular polaritons are hybridized states resulting from the strong coupling between molecular electronic states and the electromagnetic modes within the cavity. Because of their hybrid nature, molecular polaritons exhibit physical properties derived from both the molecular states and the electromagnetic modes in the cavity. The *central hypothesis* for such

enhanced transport is due to the fact that the polaritons are partially decoupled from the phonon environment[14] and assumes a larger group velocity v_g from the derivative of the hybrid dispersion curve. However, a quantitative understanding of how phonon reduces the group velocity, how the quality factor of the cavity impacts the transport, and when the ballistic to diffusive transport occurs remain open questions. Further, the electromagnetic component of these polaritons also imparts long-range coherence[21–23] and thus, enabling them to traverse in the underlying medium ballistically.[1,20,24–26]

Experimental observations reveal that the measured group velocities of molecular polaritons are lower than those predicted by their dispersion relations,[12–14,27] which is referred to as the renormalization of group velocity, likely due to the exciton-phonon coupling and cavity loss. Ultrafast measurements reported in Refs. 12 and 14 indicate an increasing deviation from the predicted velocities with an increase in the wavepacket's excitonic character. These findings underscore the importance of phonon-mediated scattering in influencing polariton transport via its excitonic component. Additionally, Ref. 13 reports that the velocities of the polariton wavepacket are strongly dependent on the cavity quality factor, $\mathcal{Q}$, despite $\mathcal{Q}$ not being explicitly related to the polariton's dispersion relation. The cavity $\mathcal{Q}$-factor, which affects the polariton's lifetime, also correlates with the polariton's coherence lifetimes[28] and hence, its transport properties, including both transient mean-square displacement (MSD) and group velocities. In particular, the transient rise of MSD[13] is due to the photonic component that propagates ballistically (which is limited by the photonic lifetime) and the dark state which is stationary.[29,30] Overall, dissipative effects that act on molecular polaritons are seen to affect both the excitonic and photonic components, thereby influencing their long-range transport. Consequently, the interplay between matter and photonic dissipation is critical in quantifying transport in practical molecular polariton systems.

Here, we examine the influence of various dissipative mechanisms on the transport properties of molecular polaritons within a one-dimensional Fabry-Pérot (FP) cavity by using the mean-field Ehrenfest (MFE) method[31] to simulate the dynamics of the hybrid light-matter system. Notably, polariton transport occurs in a collective regime where a substantial number of excitons (thousands or more) are resonantly coupled to the cavity modes, resulting in the upper polariton (UP) and lower polariton (LP) bands, as well as dark states that do not contain any significant photonic character. To faithfully model the realistic transport process, one needs to consider at least $N = 10^4 - 10^6$ molecules and $\mathcal{M} = 10^2 - 10^4$ cavity modes (that satisfy the dispersion relation), presenting a significant computational challenge.

To address the computational challenge mentioned above, we introduce a fast Fourier transform (FFT) algorithm (see Supporting Information) that leverages the symmetry of the relevant light-matter Hamiltonian to reduce the scaling (to the order of $\mathcal{O}(N \ln N)$) for the Hamiltonian matrix acting on state vector (matrix-vector multiplications) encountered during quantum dynamics propagation. We further take advantage of the stochastic Lindblad approach[31] to model the cavity loss effect, which also reduces the scaling of the dynamics propagation from $\mathcal{O}(\mathcal{M}^4)$ in Liouville space to $\mathcal{O}(\mathcal{M})$ in Hilbert space[31,32] (see Eq. S39 and Eq. S40). Finally, to solve the polariton time-dependent Schrodinger Equation (TDSE), we take advantage of the sparsity and the symmetry of the light-matter Hamiltonian to reduce the cost further.[33] The novel theoretical developments mentioned above allow us to directly simulate $N \sim 10^4$ molecules coupled to $\mathcal{M} \sim 10^2$ cavity modes, whereas previous theoretical works[28,34] are often limited by the small number of N and $\mathcal{M}$ as well as the number of trajectories that statistically converge the MQC simulations. With these tools, we numerically verify the v_g renormalization effect (Fig. 1) that has been experimentally observed in Ref. 14 and Ref. 13, the $\mathcal{Q}$-dependent transient MSD (Fig. 2) that is experimentally observed in Ref. 13, as well as the ballistic to diffusive transition (Fig. 5) that is experimentally observed in Ref. 12 and Ref. 14.

We consider the generalized Holstein-Tavis-Cummings Hamiltonian[14,35–37]

$$\hat{H} = \hat{H}_{\text{ex}} + \hat{H}_{\text{ph}} + \hat{H}_{\text{LM}} + \hat{H}_{\text{ex-b}} + \hat{H}_{\text{b}}, \quad (1)$$

where $\hat{H}_{\text{ex}}$ is the exciton Hamiltonian, $\hat{H}_{\text{ph}}$ is the Hamiltonian for cavity modes, $\hat{H}_{\text{LM}}$ is the light-matter interaction ($\text{d} \cdot \text{E}$ interactions), and $\hat{H}_{\text{b}}$ and $\hat{H}_{\text{ex-b}}$ describes the phonon bath and the exciton-bath interaction, respectively. A detailed derivation of $\hat{H}$ from the minimal coupling Hamiltonian

can be found in Eq. 102 in Ref. 35. The excitonic Hamiltonian is $\hat{H}_{\rm ex} = \sum_{n=1}^{N}(\hbar\omega_{\rm ex} + \lambda)\hat{\sigma}_n^\dagger\hat{\sigma}_n$, where $\hat{\sigma}_n^\dagger = |e_n\rangle\langle g_n|$ and $\hat{\sigma}_n = |g_n\rangle\langle e_n|$ are the raising and lowering operators for the exciton on the $n_{\rm th}$ molecule, respectively. Further, $|g_n\rangle$ and $|e_n\rangle$ are the ground state and excited state of the $n_{\rm th}$ molecule, respectively, $\hbar\omega_{\rm ex} = E_e - E_g$ is the excitation energy between the ground and excited states, and λ is the reorganization energy due to exciton-phonon coupling (caused by $\hat{H}_{\text{ex-b}} + \hat{H}_{\rm b}$ term). The $\hat{H}_{\text{ex-b}} + \hat{H}_{\rm b}$ terms further describe interactions between exciton and phonon bath, with details provided in the Supporting Information. In this work, we consider a 1D model where the molecules are evenly distributed in a box with size of $NL = 40\mu$m with $N = 10^4$, each centered at x_n, with a uniform spacing $L = x_n - x_{n-1}$, and that satisfies the boundary condition $x_{N+1} = x_1$ with $x_n = (n-1)L$ being the location of the $n_{\rm th}$ molecule.

We model the Fabry-Pérot (FP) cavity with a quasi-continuous open direction x characterized by an in-plane wavevector $k_\parallel$, and one confined direction z where $k_\perp$ is the wavevector of the fundamental mode confined between two cavity mirrors, perpendicular to the mirror surface. The frequencies of the cavity mode are given by

$$\hbar\omega_{\mathbf{k}} = \hbar c\sqrt{k_\parallel^2 + k_\perp^2}, \tag{2}$$

where c is the speed of the light and we assumed the reflective index inside the cavity is $n_{\rm c} = 1$. When $k_\parallel = 0$, $\hbar\omega_{\mathbf{k}}(0) = \hbar k_\perp = \hbar\omega_{\rm c}$ which is the cavity frequency at normal incidence. The photonic Hamiltonian $\hat{H}_{\rm ph}$ is then expressed as $\hat{H}_{\rm ph} = \sum_{\rm k_\parallel}\hbar\omega_{\mathbf{k}}(\hat{a}_{\mathbf{k}}^\dagger\hat{a}_{\mathbf{k}} + \frac{1}{2})$, where $\mathbf{k}$ is the wave vector corresponding to a given cavity mode, and $\hat{a}_{\mathbf{k}}^\dagger$ and $\hat{a}_{\mathbf{k}}$ are the photonic raising and lowering operators for mode $\mathbf{k}$, respectively. Here, we use $k_\parallel$ to index the $\mathbf{k}$ due to the constant value of $k_\perp$ for all modes considered here. We consider the cavity modes inside the same simulation box as molecules, with the size of NL along the $k_\parallel$ direction. As such, $k_\parallel$ will have discrete (but still quasi-continuous) values of $k_\alpha \equiv k_\parallel(\alpha) = \frac{2\pi}{NL}\alpha$, where the mode index is $\alpha \in [-\frac{\mathcal{M}}{2}, ...0, ...\frac{\mathcal{M}}{2}]$, and $\mathcal{M} = 10^2$ is the total number of cavity modes needed to capture the relevant energies for the hybrid system.

The light-matter interaction $\hat{H}_{\rm LM}$ term is expressed as[14,28,35,36]

$$\hat{H}_{\rm LM} = \sum_{k_\parallel}\sum_{n=1}^{N}\hbar g_{\mathbf{k}}\left(\hat{a}_{\mathbf{k}}^\dagger\hat{\sigma}_n e^{-ik_\parallel x_n} + \hat{a}_{\mathbf{k}}\hat{\sigma}_n^\dagger e^{ik_\parallel x_n}\right), \tag{3}$$

where x_n is the location of the $n_{\rm th}$ molecule.[?] Further, the $k_\parallel$-dependent light-matter coupling strength is $g_{\mathbf{k}}(k_\parallel) = g_{\rm c}\sqrt{\frac{\omega_{\mathbf{k}}}{\omega_{\rm c}}}\cos\theta$, where $g_{\rm c}$ is the single-molecule light-matter coupling strength at $k_\parallel = 0$ and is chosen as a parameter. A schematic of the model system is provided in the SI.

The transport dynamics mainly occur in the single excitation subspace

$$|E_n\rangle = |e_n\rangle\bigotimes_{m\neq n}|g_m\rangle\bigotimes_{k_\parallel\in\{k_\alpha\}}|0_{k_\parallel}\rangle \tag{4a}$$

$$|k_\alpha\rangle = |G\rangle\bigotimes_{k_\parallel\neq k_\alpha}|0_{k_\parallel}\rangle\otimes|1_{k_\alpha}\rangle \tag{4b}$$

where $|E_n\rangle$ is the single excited state for the $n_{\rm th}$ molecule located at x_n, $|k_\alpha\rangle$ is the 1-photon-dressed ground state for a photon with wave-vector component $k_\parallel = k_\alpha$, and $|G\rangle = \bigotimes_n|g_n\rangle\bigotimes_\alpha|0_{k_\alpha}\rangle$ represents the ground state for the hybrid system. We use the $\mathcal{L}$-MFE dynamics approach[31,32] to simulate the polariton transport quantum dynamics with a lossy cavity. This approach describes the exciton-photonic DOF quantum mechanically (Eq. 13), the phonon classically through the trajectory-Ehrenfest dynamics method (Eq. 14), and cavity loss through Lindblad dynamics (Eq. 15) using a stochastic approach,[31] with details provided in the Supporting Information, and key equations provided in the Method section at the end of this letter. We assume identical loss rates $\Gamma_{\rm c}$ for all cavity modes k_α, which is consistent with angle-resolved reflectance measurements of typical Fabry-Pérot cavity[38] and previous theoretical work[28] and we define the cavity quality factor at the normal incidence ($k_\parallel = 0$) as

$$\mathcal{Q} = \omega_{\rm c}/\Gamma_{\rm c}. \tag{5}$$

We describe the time-dependent polariton state with

$$|\psi(t)\rangle = \sum_{n=1}^{N}c_n(t)\,|E_n\rangle + \sum_\alpha c_\alpha(t)\,|k_\alpha\rangle\,, \tag{6}$$

where the cavity loss is incorporated by using the stochastic Lindblad approach (see Method). The

influence of phonons (from $\hat{H}_{\mathrm{ex-b}}+\hat{H}_{\mathrm{b}}$) is obtained using Ehrenfest dynamics. The spatial "wavefunction" of the time-dependent polariton state is obtained by projecting $|\psi(t)\rangle$ onto the $\langle x_n|$ basis as follows

$$\psi(x_n,t)\equiv\langle x_n|\psi(t)\rangle = c_n(t)+\frac{1}{\sqrt{N}}\sum_{\alpha}c_\alpha(t)e^{ik_\alpha x_n}, \tag{7}$$

where the photonic component is projected into the spacial grid representation, with the normalization[28] constant $1/\sqrt{N}$ because we have N spacial grid points to represent the photonic part of the polariton state. The corresponding probability density is

$$\begin{aligned}|\psi(x_n,t)|^2 =& |c_n(t)|^2+\left|\frac{1}{\sqrt{N}}\sum_{\alpha}e^{ik_\alpha x_n}c_\alpha(t)\right|^2 \\ &+2\,\mathrm{Re}\left[c_n(t)\cdot\frac{1}{\sqrt{N}}\sum_{\alpha}e^{ik_\alpha x_n}c_\alpha(t)\right],\end{aligned} \tag{8}$$

where n is the label of the molecule, x_n is the center of the mass for the n_{th} molecule, and $\sum_\alpha e^{ik_\alpha x_n}c_\alpha(t)$ is the Fourier transform of the photonic expansion coefficients from the k space to the real space. Note that the last term in Eq. 8 accounts for the interference terms of the exciton wavepacket and photonic wavepacket, which should have a significant impact on $|\psi(x_n,t)|^2$ but was ignored in the previous work.[28]

To propagate quantum dynamics, one needs to solve $i\hbar\partial|\psi(t)\rangle/\partial t=\hat{H}|\psi(t)\rangle$, where the operation $\hat{H}$ acting on $|\psi(t)\rangle$ is required, and this is computationally expensive with the standard matrix-vector multiplication when N is large. We developed a novel computational algorithm to perform the fast Fourier transform (FFT) to handle the light-matter coupling term $\hat{H}_{\mathrm{LM}}$ (Eq. 3) operating on the polariton states, with details provided in the Supporting Information (see Sec. II of the Supporting Information). We further take advantage of the sparsity of the HTC Hamiltonian to further reduce the cost of this operation,[33] with details provided in SI. Due to the quasi-linear scaling of the FFT algorithm, this approach allows an efficient simulation of $N=10^4-10^6$ molecules coupled to $\mathcal{M}=10^2-10^4$ modes.

Polariton group velocity Renormalization.

Fig. 1 illustrates the impacts of reorganization energy λ (in panel b) and cavity loss rate Γ_{c} (in panel c), on polariton group velocities v_g. Here, v_g is computed by following the *exciton character* of the wavefront of the polariton wavepacket, using the method outlined in Ref. 14, with details provided in the Supporting Information.

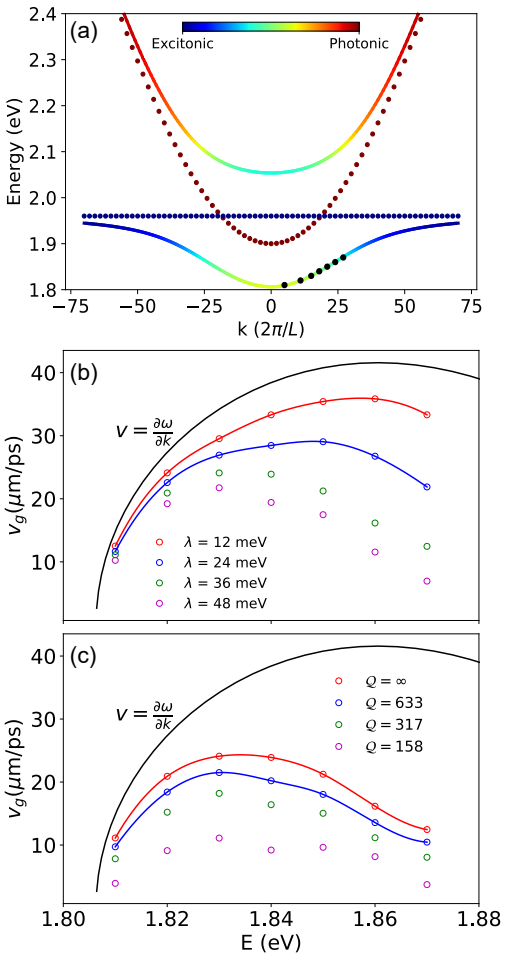

Figure 1: **Energy-resolved investigation of dissipative effects on polariton group velocity.** (**a**). Dispersion curve of the photon (red dots) and matter (blue dots) under the long-wavelength approximation.[39] (**b**). Group velocities v_g of polaritons for various reorganization energy λ in a lossless cavity. (**c**). Group velocities v_g of polaritons for different cavity quality factor $\mathcal{Q}$ with phonon reorganization energy $\lambda=36$ meV.

Fig. 1a presents the energy diagrams for the upper (UP) and lower polariton (LP) bands formed from the hybridization of the photonic band (quadratic dispersion, with $\hbar\omega_c=1.90$ eV at the normal incidence with $k_{\|}=0$) and the excitonic band (no dispersion, with $\hbar\omega_{\mathrm{ex}}=1.96$ eV). The photonic band is colored dark red and the matter branch is colored dark blue. The LP and UP bands are color-coded based on their photonic character. The collective light-matter coupling strength is $\sqrt{N}g_{\mathrm{c}}=120$ meV. These polariton states are

analytically expressed in Eq. S13 in the Supporting Information. We analyze negatively detuned molecular polaritons, where the exciton excitation energy $\hbar\omega_{\mathrm{ex}}$ exceeds the energy of a photon $\hbar\omega_c$ at normal incidence $k_{\parallel} = 0$. The initial excitation conditions are indicated in Fig. 1 using black dots on the lower polariton branch, corresponding to a laser pulse with a narrow energy bandwidth (to model the experimental condition in Ref. 14), and this is associated with a narrow width on a certain $k_{\parallel}$ on the lower polariton (LP) dispersion curve. Theoretical details on simulating these initial conditions are provided in the Supporting Information.

Fig. 1b shows group velocity v_g with different initial energies (corresponding to different $k_{\parallel}$) as shown in Fig. 1a. Here, the cavity is lossless, with $\Gamma_{\mathrm{c}} = 0$. The solid black line indicates the group velocity obtained as $v_g = \partial\hbar\omega_-/\partial k_{\parallel}$, which is the gradient of the dispersion curve and is the theoretical limit of v_g on the lower polariton branch ω_- in a lossless cavity without coupling to the phonons (vibrations). The open circles with different colors are v_g for the excitonic system with different reorganization energy λ, which indicates the overall coupling strength between excitons and phonon vibrations. It is evident that as λ increases, v_g decreases overall, indicating that the polaritons propagate at a reduced v_g (compared to the theoretical limit $\partial\hbar\omega_-/\partial k_{\parallel}$) due to increased exciton-phonon coupling. This reduction of v_g due to exciton-phonon coupling was referred to as the group velocity renormalization.[14] Increasing exciton-phonon coupling λ increases the dynamical disorder (homogeneous disorder) within the light-matter hybrid system. As interpreted in Ref. 14, this leads to an increased dynamical *transient localization* that impedes ballistic polariton transport. Further, the magnitude of the v_g renormalization increases with increasing polariton energy E (or accordingly, $k_{\parallel}$). This is because the excitonic character of the wavepacket on the lower polariton branch increases as E increases (see Fig. 1). Consequently, the deviation of v_g is attributed to the increased excitonic character which couples to the phonon that makes polariton transport more susceptible to exciton-phonon coupling. The photonic component does not directly couple to the phonon and thus at a lower value of E, the magnitude of the v_g renormalization is smaller. Similar experimental observations are found in earlier work,[14] with layered halide perovskite coupled to the cavity.

Figure 1c illustrates the effects of cavity loss on v_g by changing the $\mathcal{Q}$ factor (photonic loss rate Γ_{c}). In this panel, the reorganization energy is fixed at $\lambda = 36$ meV. With a decreasing $\mathcal{Q}$ (increasing Γ_{c}), v_g further decreases due to a more rapid attenuation of the photonic contribution to the polariton wavepacket due to cavity loss, which is responsible for the ballistic motion of the wavepacket. Thus, a larger Γ_{c} inhibits ballistic transport and further reduces the group velocity of the polariton v_g. Although the effects of Γ_{c} on v_g will depend on the photonic character of the polariton wavepacket, the renormalization of v_g happens across the whole range of E and is less sensitive to the photonic character contribution (as compared to Fig. 1b where v_g reduction strongly depends on the exciton character). This is likely due to the fact that regardless of the photonic contribution in a given polariton wavepacket, the photonic part is almost solely responsible for ballistic propagation, and the cavity loss will decrease the photonic excitation and thus v_g.

Cavity Quality-factor dependent transport

Fig. 2a presents the impact of the cavity loss rate on the group velocities of polaritons v_g with a broadband excitation on the upper polariton (UP) band (indicated with the gray Gaussian wavepacket in the inset of Fig. 2a), to model the similar experimental condition in Ref. 13. For the initial excitation, an energy bandwidth that encompasses the majority of the UP band, from 2.02 eV to 2.62 eV (see scales in Fig. 1a), was selected. The resulting wavepacket is localized, with a mean squared displacement (MSD) of 0.137 $\mu\mathrm{m}^2$. Here, we use $\lambda = 36$ meV, and vary the $\mathcal{Q}$ factor. As shown in Fig. 2, v_g increases with increasing $\mathcal{Q}$, achieving a maximum value of about 132.5 μm/ps as $\mathcal{Q} \to \infty$. Our results demonstrate a trend consistent with experimental measurements in Ref. 13 (see Fig. 2e of that work) which examined polariton transport in the BODIPY-cavity system with varying $\mathcal{Q}$-factors.

Fig. 2b presents the transient MSD σ^2 of a polariton wavepacket under various $\mathcal{Q}$-factors. Experimentally, the transient MSD is derived from transient absorption signals measured by probing differences in the transmittance of the sample,[13,28] providing a measure of the polariton wavepacket's

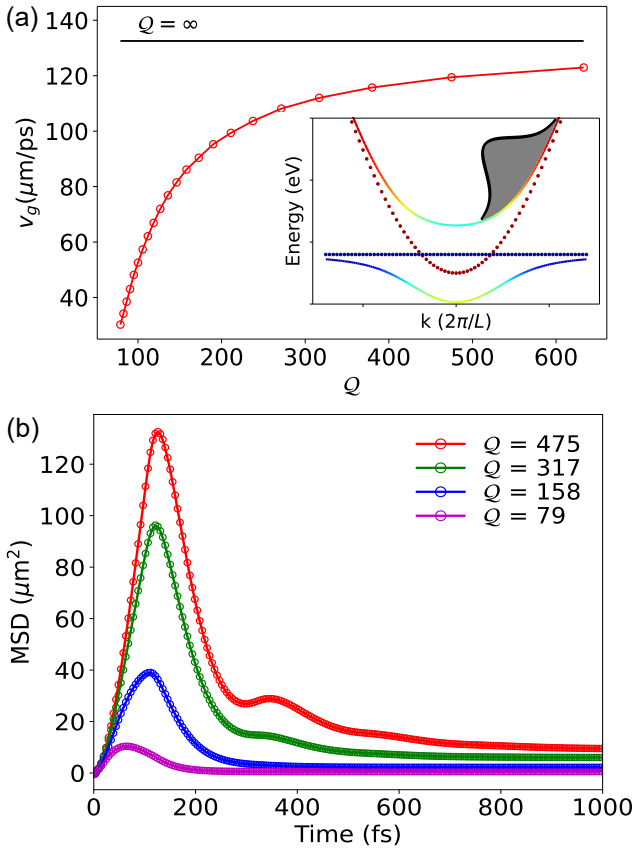

Figure 2: **Group velocity dependence on quality-factor for UP broadband excitation. a** Polariton group velocity v_g vs cavity quality factor $\mathcal{Q}$. The inset figure shows the energy bandwidth used for the initial excitation in the UP branch, optimizing the localization of the polariton wavepacket. Results are converged with 250 trajectories, validated against a set of runs with 1000 trajectories. **b** Time-dependent transient MSD with UP initial excitation for various $\mathcal{Q}$.

spread. It can be theoretically computed as[28,34]

$$\sigma^2(t) = \langle\psi(t)|(\hat{x} - \langle x\rangle)^2|\psi(t)\rangle \tag{9}$$
$$= \sum_{n=1}^{N} |\psi(x_n, t)|^2 \cdot (x_n - \langle x\rangle)^2,$$

where $\langle x\rangle$ is the centroid of the initial polariton wavepacket (at $t = 0$) in position space, and $|\psi(x_n, t)|^2$ is expressed in Eq. 8. Further, $|\psi(x_n, t)|^2 = |\langle x_n|\psi(t)\rangle|^2$ is the population density of the polaritonic wavepacket at the n_{th} site, obtained from Eq. 8.

As shown in Fig. 2b, in a very lossy cavity $\mathcal{Q}$ = 79 (magenta curve), the wavepacket shows minimal spread within a brief duration of time for t ∼50 fs), and its MSD decreases below its initial value (*i.e.*, contraction) after a long time (∼1 ps). With an increase in the $\mathcal{Q}$-factor, both the wavepacket's maximum MSD and the corresponding rise time increase. The initial rise of MSD is attributed to the photonic character in polariton, which is responsible for ballistic transport, as pointed out by recent theoretical work.[28] The dip of the MSD right after the initial rise is attributed to both the decay of the UP population to the dark states, as well as the cavity loss, which are competing at a similar time scale, with theoretical details provided in Fig. 4. We note that the steady-state MSD in lossy cavities with $\mathcal{Q} > 158$ surpasses the MSD of the original polariton wavepacket, suggesting that strong light-matter coupling (here, $\sqrt{N}g_c = 120$ meV) facilitates the expansion of the underlying excitons over a larger volume even in the presence of cavity loss. The observed trends in our numerical simulations are consistent with the transient absorption measurements in BODIPY-R molecules that are strongly coupled to an FP cavity (see Fig. 2c in Ref. 13).

Fig. 3a presents a similar study of how $\mathcal{Q}$-factor impacts the group velocities v_g of polaritons, but with a broadband excitation on the lower polariton (LP) branch (see gray Gaussian initial excitation on the LP branch in the inset). For the LP initial excitation, an energy bandwidth that covers most of the LP band was selected, ranging from 1.8 eV to 1.95 eV. As demonstrated in Fig. 3, v_g increases with increasing $\mathcal{Q}$, reaching a maximum value of about 30 μm/ps as $\mathcal{Q} \to \infty$. We note that the maximum attainable velocity for an LP wavepacket is lower than that for an UP wavepacket. This is largely due to the curvature of the polariton dispersion curve, where steeper slopes for UP lead to larger group velocities. In particular, the LP v_g has a theoretical limit of $\partial\hbar\omega_-/\partial k_\parallel$, which is lower compared to the UP excitation whose theoretical limit of group velocity $\partial\hbar\omega_+/\partial k_\parallel$ is larger. The exciton-phonon coupling λ and cavity loss Γ_c further reduce the value of v_g, but the upper bound of v_g is largely dictated by the dispersion curvature.

Fig. 3b presents the transient MSD computed from Eq. 9 with the LP initial excitation. In contrast to UP initial excitation (see Fig. 2b), the transient MSDs for an LP wavepacket excitation exhibit an increase followed by stabilization over time, without further collapse of the polariton wavepacket. Increasing the $\mathcal{Q}$-factor results in corresponding increases in both the wavepacket's steady-state MSD and the associated rising time. To the best of our knowledge, there are no direct

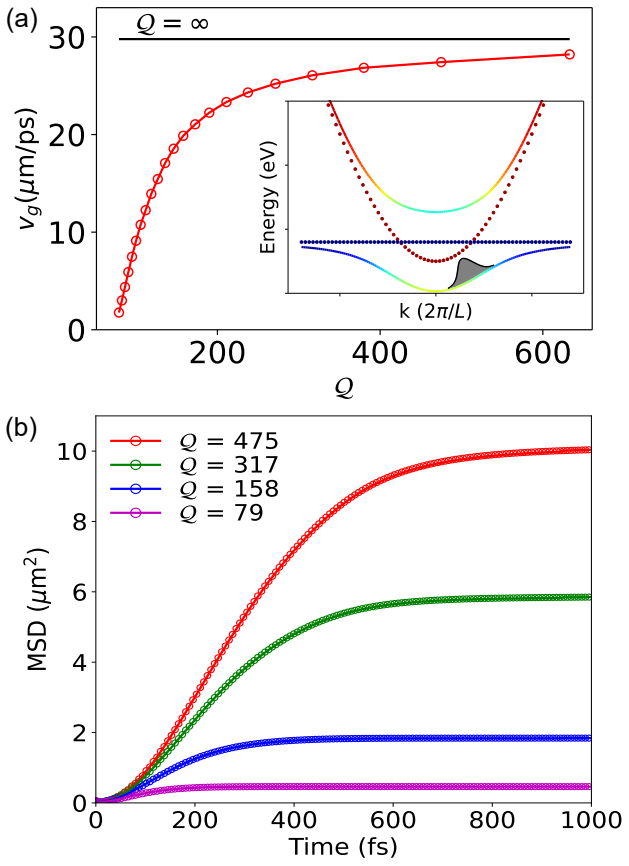

Figure 3: **Group velocity dependence on quality-factor for LP broadband excitation.** **a** Polariton group velocity v_g vs cavity quality factor $\mathcal{Q}$. The inset figure illustrates the energy bandwidth used for the initial excitation while maximizing the localization of the polariton wavepacket. **b** Time-dependent transient MSD with LP initial excitation for various $\mathcal{Q}$.

experimental measurements to verify the behavior of Fig. 3b, and the same experimental setup in Ref. 13 could be used to verify this behavior once the initial excitation is set to be on LP. In the section below, we investigate the polariton quantum dynamics and time-dependent polariton wavepacket and dark state wavepacket (exciton wavepacket) to interpret the different behavior of transient MSD in Fig. 2 and Fig. 3

Quantum Dynamics in Polariton Transport process

We provide a comprehensive investigation of polariton group velocities and transient MSD by analyzing the corresponding populations of the polariton wavepackets and dark exciton wavepackets, for both UP and LP initial excitations. Here, we consider a high $\mathcal{Q} = 475$, while the same analysis for a lower $\mathcal{Q} = 79$ is provided in the Supporting Information.

Fig. 4a and Fig. 4b present the population dynamics of the UP (blue), LP (red), and dark states (black) under a broadband UP excitation and broadband LP excitation, respectively (same as in Fig. 2 and Fig. 3) with cavity quality factors of $\mathcal{Q} = 475$. The ground state population (green) is also depicted, due to the cavity loss. The definitions of UP, LP, and Dark states are provided in Eqs. S12-13 of the Supporting Information. In Fig. 4a, an initial substantial decrease in the UP population is observed, accompanied by a sharp increase in the dark state population and a slower rate of increase in the ground state population. The population transfer from the UP to the dark state is mediated by exciton-phonon coupling,[40,41] and the population transfer to the ground state is attributed to cavity loss. Here, with a low cavity loss rate (high $\mathcal{Q}$), it is evident that exciton-phonon coupling has a more pronounced influence on the decay of the initial UP state population than cavity loss. In the case of a broadband LP excitation, as shown in Fig. 4, an initial substantial decrease in the LP population is observed, and the rate of population transfer from LP to the ground state is similar to the rate of population transfer from LP to the dark states. In both scenarios, the populations of the LP for a broadband UP excitation and the populations of the UP for a broadband LP excitation are negligible, which agrees with previous findings showing that transitions from UP/LP to dark state are much faster compared to from dark state to UP/LP.[23,40,41] The rapid decrease in the UP and LP populations corroborate the results in Fig. 2 and Fig. 3 respectively, where a swift depletion of the UP and LP populations, containing the photonic component, results in reduced ballistic transport, as evidenced by the transient MSD. This also explains the Q-dependent v_g.

The different behaviors of transient MSD in Fig. 2b and Fig. 3b are further elucidated by examining the polariton wavepacket and the dark exciton density in position space, as depicted in Fig. 4c and Fig. 4d for broadband UP and LP excitation respectively. The initial wavepacket is centered at $x = 20$ μm and the total simulation spans $x \in [0, 40]$ μm, with the predominant characters of UP or LP. Over time, the UP and LP wavepacket propagates outward from the center, as seen from the UP and LP population densities (6 fs to 153 fs), primarily due to their *photonic charac-*

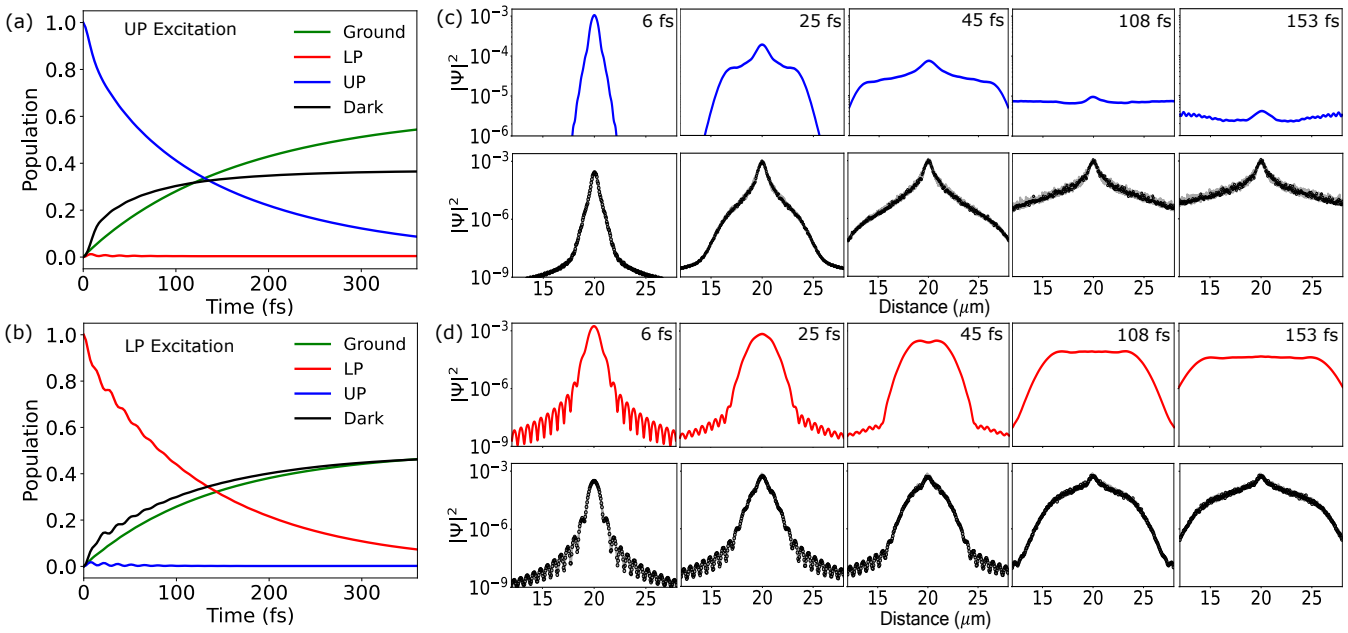

Figure 4: **Polariton population dynamics and wavepacket.** The populations of UP (blue), LP (red), dark (black), and ground states (green) are presented, with **a** broadband UP excitation and **b** broadband LP excitation. The wavepackets in position space, decomposed into polariton and dark state components, are illustrated for (**c**) broadband UP excitation and for (**d**) broadband LP excitation.

ter which does not directly couple to the phonons, and exhibit ballistic transport. Due to exciton-phonon coupling, the UP and LP wavepacket transfers the population to the dark state, resulting in an increase in the dark state probability densities. Moreover, the resultant dark state wavepacket is relatively immobile, as it consists of excitons that are governed by highly diffusive transport (and also due to its dispersionless band that we put in the model). The *intuitive picture* of polariton transport[1] is thus that polariton wavepacket exhibits a fast, ballistic propagation in space, and as it moves, it "drags" the dark exciton wavepacket with it through polariton to dark state population transfer. As the polariton wavepacket moves, it will eventually disappear due to cavity loss (and transition to dark states), but the dark excitons will be robust against cavity loss and stay extended in space.

Due to the larger v_g of the UP wavepacket, the polariton wavepacket expands rapidly in early time, contributing to a sharp rise in the total transient MSD (Fig 2b). For example, we see at $t = 45$ fs that the UP wavepacket has already spread to a width spanning from 15 μm to 25 μm. Consequently, the UP wavepacket (blue curve in Fig. 4c) propagates more rapidly than the dark state wavepacket (black curve in Fig. 4c), indicating that the rate of population transfer from the UP wavepacket to the dark states at a particular spatial location is slower than the rate of propagation of the UP wavepacket. Note that the dark exciton in our model, in principle, has $v_g = 0$ from the derivative of the dispersion curve. The effective propagation of the dark exciton wavepacket is largely due to the transfer of population from UP which propagates ballistically in space at an early time. After $t = 108$ fs, the UP wavepacket is further spread out and its amplitude also starts to decrease due to cavity loss, resulting in a decrease in its magnitude, as well as its contribution to the transient MSD. These observations explain the behavior of the MSD as shown in Fig. 2b, where the MSD initially increases to a peak value before declining.

In contrast, for the LP wavepacket, Fig. 4d shows a more gradual expansion of the polariton wavepacket. For instance, at $t = 45$ fs, the LP wavepacket (red curves) spans a width ranging from about 18 μm to 22 μm only, which is akin to the width of the corresponding dark state wavepacket at $t = 45$ fs. As a result, the LP wavepacket advances at a rate comparable to the rate of LP to dark state transition, resulting in a synchronized expansion of both LP and dark ex-

[1]This was pointed out by Milan Delor to us through private communications.

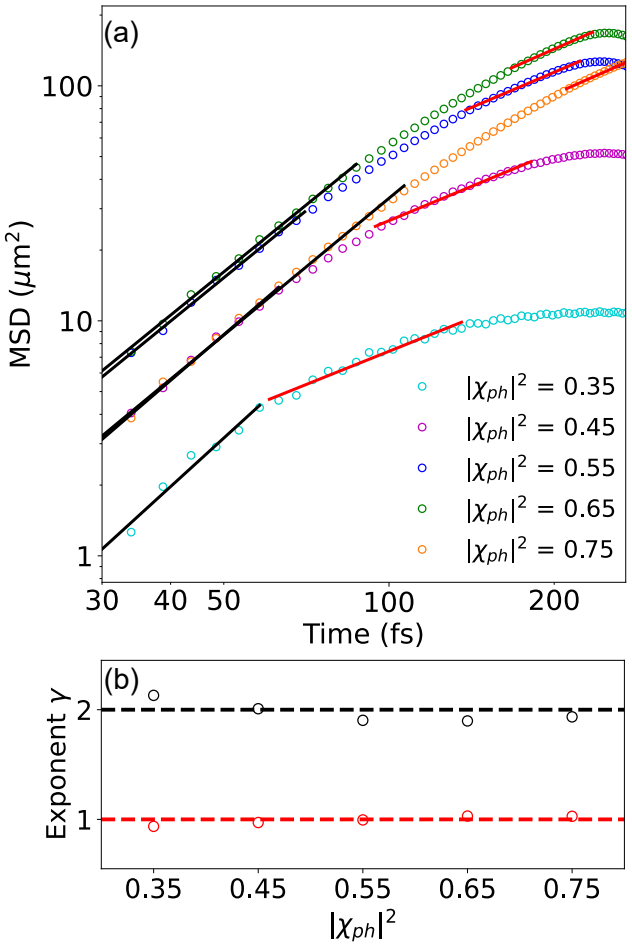

Figure 5: **Ballistic transport to the diffusive transport.** (**a**) MSD for the polariton as a function of time, with various photonic character $|\chi_{\rm ph}|^2$. (**b**) The exponents extracted from fitting the MSDs with various photonic character $|\chi_{\rm ph}|^2$ with Eq. (10).

citon wavepacket. This leads to a steady increase in the transient MSD followed by stabilization as depicted in Fig. 3b.

Transition from ballistic to diffusive transport

We investigate the behavior of polariton transport due to the influence of the photonic character from the initial wavepacket at $t = 0$. Here, we consider $\lambda = 36$ meV, and $\mathcal{Q} = 633$ (which is in line with the cavity used in Ref. 12). We also consider a narrow band of initial excitation conditions with a narrow range of $k_\parallel$ (or the corresponding energy window) on the lower polariton state (see Fig. 1a), to model the experimental conditions in Ref. 14 and Ref. 12 However, we use a cavity with a lower frequency for this study ($\hbar\omega_c = 1.77$ eV at the normal incidence for $k_\parallel = 0$), which is more red-detuned compared to the curve presented in Fig. 1a. For each initial excitation condition with a given $k_\parallel$, we report the corresponding photonic characters $|\chi_{\rm ph}|^2 = \sum_\alpha |c_\alpha(t=0)|^2$ of the wavepacket, defined as the sum of the photonic components of the polariton wavepacket (see Eq. 12) at $t = 0$. To determine the transport characteristics, we perform a least-square fitting of the transient MSD with the equation

$$\sigma^2(t) = \sigma^2(t_0) + D \cdot t^\gamma, \tag{10}$$

which corresponds to a generalized diffusion equation.[12,42] The constant D represents the generalized diffusion coefficient, while the exponent γ characterizes the transport properties. For $\gamma = 1$, the transport is diffusive, and for $\gamma = 2$, the transport is ballistic,[12,14] and for $\gamma < 1$, the transport is sub-diffusive.[43]

Fig. 5a presents the time-dependent MSD (Eq. 9) as a function of time in a log-log scale. We find that there are two separate transport stages, one in the early time with $\gamma \approx 2$ (with black solid lines as the fitting lines) and one in later time, with $\gamma \approx 1$ (red solid lines). Fig. 5b, provides the value of γ as a function of $|\chi_{\rm ph}|^2$, obtained from the fitting in panel a. The duration of the ballistic stage depends on the photonic character of the wavepacket. For small photonic characters ($|\chi_{\rm ph}|^2 = 0.35$), the ballistic stage last for up to 60 fs while for large photonic characters ($|\chi_{\rm ph}|^2 = 0.75$), the ballistic stage last for a longer duration of up to 100 fs. Further, the time when the wavepacket transitions from ballistic to diffusive transport happens at earlier times as $|\chi_{\rm ph}|^2$ decreases. This suggests that for the initial polariton wavepacket, the transport is ballistic for a duration (with v_g being renormalized by exciton-phonon coupling and cavity loss), before gradually becoming diffusive. This observation is in close agreement with recent experiments (*e.g.*, Fig. 2c in Ref. 14 and Fig. 4 in Ref. 12).

Note that even under the diffusive transport stage ($\gamma \approx 1$) the group velocity is still much larger than the expected gradient of matter dispersion (which is 0 in the current model). Also, the absolute value of MSD depends on the group velocity, and with a large photonic contribution $|\chi_{\rm ph}|^2 = 0.75$, the gradient of the LP dispersion is relatively small (close to a small $k_\parallel$ value in FP cavity as indicated in Fig. 1a). As such, for $|\chi_{\rm ph}|^2 = 0.75$, even though the transport is ballistic for the longest time (for $t < 100$ fs) compared to the other cases investigated here, the MSD is

not necessarily the largest. Ideally, one would like to have a molecule cavity system that simultaneously gives a reasonably large photonic contribution $|\chi_{\rm ph}|^2$ and a large gradient of the polariton band $\partial\omega_-/\partial k_\parallel$. While this is not easy to accomplish for the LP band of an FP cavity (see Fig. 1), it is possible to have a reasonably large value of both for a different type of cavity.[44]

Conclusions

We developed an efficient simulation approach for investigating polariton transport quantum dynamics simulations. This approach describes exciton and photonic DOF quantum mechanically, the phonon DOFs quasi-classically, and cavity loss at the level of Lindblad quantum Master Equations. The computational approach includes a fast Fourier transform algorithm to efficiently handle the light-matter interactions part of the Hamiltonian, taking advantage of the sparsity of the Hamiltonian for efficient quantum dynamics propagations,[33] and a stochastic Lindblad algorithm to model cavity loss.[31] By employing these techniques, we have achieved quasi-linear scaling for our quantum dynamical method, enabling simulations of thousands, and even over a million, degrees of freedom within the system of interest. It allows us to directly stimulate $N = 10^4$ molecules collectively coupled to $\mathcal{M} = 10^2$ cavity modes in a generalized Holstein-Tavis-Cummings Hamiltonian (see Eq. 11) and investigate polariton transport dynamics from direct simulations of various recent polariton experiments of relevance.[12–14]

We performed direct simulations to investigate the impact of dissipative mechanisms, such as exciton-phonon coupling and cavity loss, on the dynamics of polariton transport. The simulations revealed a decrease in polariton group velocities with increasing cavity loss for both narrowband (Fig. 1c) and broadband excitations (Figs. 2-3), attributed to the reduction in photon populations that facilitate ballistic transport of the polariton wavepacket. This agrees with the experimental results in Ref. 13. Furthermore, the simulations show a decrease in polariton velocities with increasing exciton-phonon coupling, where phonon scattering introduces additional friction, thereby slowing down the polariton wavepacket, agreeing with the experimental observation in Ref. 14. Additionally, the transient MSD of polariton wavepackets upon a UP broadband excitation demonstrates transient growth and then contraction, agreeing with the experimental observation in Ref. 13. This is due to the very fast expansion of the UP polariton wavepacket in space and the relatively slower rate of transitions to the dark exciton wavepacket, as demonstrated by our quantum dynamics analysis (Fig. 4). From the transient MSD, we were able to analyze the transport characteristics of the wavepacket that illustrates a ballistic-to-diffusive turnover, which has been experimentally observed in Ref. 14 and Ref. 12. Overall, the results from our quantum dynamics simulations successfully captured all the trends observed in recent polariton transport experiments.[12–14]

Our theoretical simulation predicts that with an LP broadband excitation, one should be able to see the $\mathcal{Q}$-factor dependence of the transient MSD, but it will not further contract in a longer time due to a more synchronized LP polariton expansion and transition to the dark excitons. This prediction can be checked experimentally with the same techniques reported in Ref. 13. Our work paves the way for a systematic investigation and understanding of polariton transport phenomena.

Method

We briefly outline the $\mathcal{L}$-MFE approach used in this work to propagate polariton transport quantum dynamics. Using the single excitation basis in Eq. 4, the quantum part of the GHTC Hamiltonian (Eq. 1) $\hat{H}_{\rm Q} = \hat{H} - \hat{H}_{\rm b}$ is expressed as

$$\hat{H}_{\rm Q}(\mathbf{R}) = \sum_n \hbar\omega_n \left|E_n\right\rangle\!\left\langle E_n\right| + \sum_\alpha \hbar\omega_\alpha \left|k_\alpha\right\rangle\!\left\langle k_\alpha\right| \quad (11)$$
$$+ \sum_{n\alpha} g_{\rm c}(k_\alpha) \left(\left|E_n\right\rangle\!\left\langle k_\alpha\right| e^{-ik_\alpha x_n} + \left|k_\alpha\right\rangle\!\left\langle E_n\right| e^{ik_\alpha x_n}\right)$$

where $\hbar\omega_n = \hbar\omega_{\rm ex} + \lambda + \sum_\nu c_{n,\nu} R_{n,\nu}$ (here, $R_{n,\nu}$ is the $\nu_{\rm th}$ bath mode in molecule n, and $c_{n,\nu}$ is the coupling strength between the bath and exciton $|e_n\rangle$), and $\hbar\omega_\alpha = \hbar c\sqrt{k_\alpha^2 + k_\perp^2}$ is the cavity mode frequency. We describe the time-dependent quantum state in the exciton-photon subspace as

$$\left|\Psi(t)\right\rangle = \sum_{n=1}^{N} c_n(t)\left|E_n\right\rangle + \sum_\alpha c_\alpha(t)\left|k_\alpha\right\rangle + c_0(t)|G\rangle, \quad (12)$$

where $c_n(t)$ and $c_\alpha(t)$ are the excitonic and photonic expansion coefficients, and $c_0(t)$ is the coefficient for the ground state (that captures cavity loss). The polariton quantum dynamics is propagated with

$$i\hbar\frac{\partial}{\partial t}|\Psi(t)\rangle = \hat{H}_{\rm Q}(\mathbf{R})|\Psi(t)\rangle, \quad (13)$$

where $|\Psi(t)\rangle$ is represented using Eq. 12. The bath DOF $\mathbf{R}$, on the other hand, is propagated classically, governed by the time-dependent mean-field force

$$\mathbf{F} = -\nabla_{\mathbf{R}} \left[\langle \Psi(t) | \hat{H}_{\mathrm{ex-b}}(\mathbf{R}) | \Psi(t) \rangle + H_{\mathrm{b}}(\mathbf{R}) \right]. \quad (14)$$

The cavity loss (photon loss) dynamics from state $|k_\alpha\rangle$ to state $|G\rangle$ is formally described using the Lindblad super operator $\hat{L}_\alpha = |G\rangle\langle k_\alpha|$. The dissipator $\mathcal{L}$ accounts for the cavity loss channel causing the system to relax

$$\mathcal{L}[\hat{\rho}_{\mathrm{Q}}] = \sum_\alpha \Gamma_{\mathrm{c}} \Big(\hat{L}_\alpha \hat{\rho}_{\mathrm{Q}} \hat{L}_\alpha^\dagger - \frac{1}{2} \{ \hat{L}_\alpha^\dagger \hat{L}_\alpha, \hat{\rho}_{\mathrm{Q}} \} \Big), \quad (15)$$

where Γ_{c} is the cavity loss rate (which we assume to be the same for all k_α photonic modes, $\{\hat{A}, \hat{B}\} = \hat{A}\hat{B} + \hat{B}\hat{A}$ is the anti-commutator, and $\hat{\rho}_{\mathrm{Q}} = \mathrm{Tr}_{\mathrm{b}}[\hat{\rho}] = |\Psi(t)\rangle\langle\Psi(t)|$ is the reduced density matrix operator for the quantum subsystem, which described the mixed state upon trajectory average. To reduce the cost of performing Eq. 15, the stochastic algorithm[31] is used, where the photonic coefficients c_α are updated as $c_\alpha(t + dt) = c_\alpha(t) e^{-\Gamma_{\mathrm{c}} dt}$, and the coefficients of the ground state change by the amount $c_0(t + dt) = e^{i\phi} \sqrt{|c_0(t)|^2 + (1 - e^{-\Gamma_\alpha dt}) |c_\alpha(t)|^2}$, where ϕ is a random phase with details provided in the Supporting Information.

Simulation Details. For all simulations, $N = 10001$ molecules and $\mathcal{M} = 283$ modes were chosen, keeping the ratio of $N/\mathcal{M} \approx 35$. The inter-molecular spacing is set to be $L = 40$ Å, and the total light-matter coupling strength is set to $\sqrt{N} g_{\mathrm{c}} = 120$ meV. All results are obtained with an ensemble of 250 independent trajectories. Convergence tests are performed with up to 1000 trajectories. The nuclear time step used in $\mathcal{L}$-MFE method is $\Delta t = 2.5$ fs, where during each nuclear propagation, there are 100 electronic propagation steps with a time step $dt = 0.025$ fs. The nuclear EOM is numerically integrated with the velocity verlet algorithm and the TDSE is solved with the RK4 algorithm.

Acknowledgement Computational resources were provided by the Center for Integrated Research Computing (CIRC) at the University of Rochester. The authors thank Mike Taylor for making the TOC Figure. The authors appreciate valuable discussions and comments from Eric Koessler, Braden Weight, Arkajit Mandal, Michael Taylor, and Wenxiang Ying. P. H. appreciates valuable discussions with Andrew Musser, Tal Schwartz, and Milan Delor.

References

(1) Liu, B.; Huang, X.; Hou, S.; Fan, D.; Forrest, S. R. Photocurrent generation following long-range propagation of organic exciton–polaritons. *Optica* **2022**, *9*, 1029–1036.

(2) Hains, A. W.; Liang, Z.; Woodhouse, M. A.; Gregg, B. A. Molecular semiconductors in organic photovoltaic cells. *Chemical reviews* **2010**, *110*, 6689–6735.

(3) Gather, M. C.; Köhnen, A.; Meerholz, K. White organic light-emitting diodes. *Advanced Materials* **2011**, *23*, 233–248.

(4) Reineke, S.; Lindner, F.; Schwartz, G.; Seidler, N.; Walzer, K.; Lüssem, B.; Leo, K. White organic light-emitting diodes with fluorescent tube efficiency. *Nature* **2009**, *459*, 234–238.

(5) Reineke, S.; Thomschke, M.; Lüssem, B.; Leo, K. White organic light-emitting diodes: Status and perspective. *Reviews of Modern Physics* **2013**, *85*, 1245.

(6) Ginsberg, N. S.; Tisdale, W. A. Spatially resolved photogenerated exciton and charge transport in emerging semiconductors. *Annual review of physical chemistry* **2020**, *71*, 1–30.

(7) Lunt, R. R.; Giebink, N. C.; Belak, A. A.; Benziger, J. B.; Forrest, S. R. Exciton diffusion lengths of organic semiconductor thin films measured by spectrally resolved photoluminescence quenching. *Journal of Applied Physics* **2009**, *105*.

(8) Liang, C.; Zhao, D.; Li, P.; Wu, B.; Gu, H.; Zhang, J.; Goh, T. W.; Chen, S.; Chen, Y.; Sha, Z., et al. Simultaneously boost diffusion length and stability of perovskite for high performance solar cells. *Nano Energy* **2019**, *59*, 721–729.

(9) Adhyaksa, G. W.; Veldhuizen, L. W.; Kuang, Y.; Brittman, S.; Schropp, R. E.; Garnett, E. C. Carrier diffusion lengths in hybrid perovskites: processing, composition, aging, and surface passivation effects. *Chemistry of Materials* **2016**, *28*, 5259–5263.

(10) Yang, D.; Ma, D. Development of organic semiconductor photodetectors: from mechanism to applications. *Advanced optical materials* **2019**, *7*, 1800522.

(11) Forrest, S. R. Active optoelectronics using thin-film organic semiconductors. *IEEE Journal of Selected Topics in Quantum Electronics* **2000**, *6*, 1072–1083.

(12) Balasubrahmaniyam, M.; Simkhovich, A.; Golombek, A.; Sandik, G.; Ankonina, G.; Schwartz, T. From enhanced diffusion to ultrafast ballistic motion of hybrid light–matter excitations. *Nature Materials* **2023**, *22*, 338–344.

(13) Pandya, R.; Ashoka, A.; Georgiou, K.; Sung, J.; Jayaprakash, R.; Renken, S.; Gai, L.; Shen, Z.; Rao, A.; Musser, A. J. Tuning the coherent propagation of organic exciton-polaritons through dark state delocalization. *Advanced Science* **2022**, *9*, 2105569.

(14) Xu, D.; Mandal, A.; Baxter, J. M.; Cheng, S.-W.; Lee, I.; Su, H.; Liu, S.; Reichman, D. R.; Delor, M. Ultrafast imaging of polariton propagation and interactions. *Nature Communications* **2023**, *14*, 3881.

(15) Jin, L.; Sample, A. D.; Sun, D.; Gao, Y.; Deng, S.; Li, R.; Dou, L.; Odom, T. W.; Huang, L. Enhanced two-dimensional exciton propagation via strong light–matter coupling with surface lattice plasmons. *ACS Photonics* **2023**, *10*, 1983–1991.

(16) Berghuis, A. M.; Tichauer, R. H.; de Jong, L. M.; Sokolovskii, I.; Bai, P.; Ramezani, M.; Murai, S.; Groenhof, G.; Gomez Rivas, J. Controlling exciton propagation in organic crystals through strong coupling to plasmonic nanoparticle arrays. *ACS photonics* **2022**, *9*, 2263–2272.

(17) Pekar, S. The theory of electromagnetic waves in a crystal in which excitons are produced. *Sov. Phys. JETP* **1958**, *6*, 4.

(18) Kavokin, A.; Malpuech, G. *Cavity polaritons*; Elsevier, 2003.

(19) Weisbuch, C.; Nishioka, M.; Ishikawa, A.; Arakawa, Y. Observation of the coupled exciton-photon mode splitting in a semiconductor quantum microcavity. *Physical review letters* **1992**, *69*, 3314.

(20) Coles, D. M.; Somaschi, N.; Michetti, P.; Clark, C.; Lagoudakis, P. G.; Savvidis, P. G.; Lidzey, D. G. Polariton-mediated energy transfer between organic dyes in a strongly coupled optical microcavity. *Nature materials* **2014**, *13*, 712–719.

(21) Shi, L.; Hakala, T.; Rekola, H.; Martikainen, J.-P.; Moerland, R.; Törmä, P. Spatial coherence properties of organic molecules coupled to plasmonic surface lattice resonances in the weak and strong coupling regimes. *Physical review letters* **2014**, *112*, 153002.

(22) Chen, Y.; Shi, Y.; Gan, Y.; Liu, H.; Li, T.; Ghosh, S.; Xiong, Q. Unraveling the Ultrafast Coherent Dynamics of Exciton Polariton Propagation at Room Temperature. *Nano Letters* **2023**, *23*, 8704–8711.

(23) Chng, B. X.; Ying, W.; Lai, Y.; Vamivakas, A. N.; Cundiff, S. T.; Krauss, T.; Huo, P. Mechanism of Polariton Decoherence in the Collective Light-Matter Couplings Regime. **2024**,

(24) Steger, M.; Liu, G.; Nelsen, B.; Gautham, C.; Snoke, D. W.; Balili, R.; Pfeiffer, L.; West, K. Long-range ballistic motion and coherent flow of long-lifetime polaritons. *Physical Review B* **2013**, *88*, 235314.

(25) Hou, S.; Khatoniar, M.; Ding, K.; Qu, Y.; Napolov, A.; Menon, V. M.; Forrest, S. R. Ultralong-range energy transport in a disordered organic semiconductor at room temperature via coherent exciton-polariton propagation. *Advanced Materials* **2020**, *32*, 2002127.

(26) Orgiu, E.; George, J.; Hutchison, J.; Devaux, E.; Dayen, J.; Doudin, B.; Stellacci, F.; Genet, C.; Schachenmayer, J.; Genes, C., et al. Conductivity in organic semiconductors hybridized with the vacuum field. *Nature Materials* **2015**, *14*, 1123–1129.

(27) Rozenman, G. G.; Akulov, K.; Golombek, A.; Schwartz, T. Long-range transport of organic exciton-polaritons revealed by ultrafast microscopy. *ACS photonics* **2018**, *5*, 105–110.

(28) Tichauer, R. H.; Sokolovskii, I.; Groenhof, G. Tuning the Coherent Propagation of Organic Exciton-Polaritons through the Cavity Q-factor. *Advanced Science* **2023**, *10*, 2302650.

(29) Sokolovskii, I.; Tichauer, R. H.; Morozov, D.; Feist, J.; Groenhof, G. Multi-scale molecular dynamics simulations of enhanced energy transfer in organic molecules under strong coupling. *Nature Communications* **2023**, *14*, 6613.

(30) Sokolovskii, I.; Groenhof, G. Photochemical initiation of polariton-mediated exciton propagation. *Nanophotonics* **2024**,

(31) Koessler, E. R.; Mandal, A.; Huo, P. Incorporating Lindblad decay dynamics into mixed quantum-classical simulations. *The Journal of Chemical Physics* **2022**, *157*.

(32) Mondal, M. E.; Koessler, E. R.; Provazza, J.; Vamivakas, A. N.; Cundiff, S. T.; Krauss, T. D.; Huo, P. Quantum dynamics simulations of the 2D spectroscopy for exciton polaritons. *The Journal of Chemical Physics* **2023**, *159*.

(33) Mondal, E.; Vamivakas, N.; Cundiff, S.; Krauss, T.; Huo, P. Polariton Spectra under the Collective Coupling Regime. I. Efficient Simulation of Linear Spectra and Quantum Dynamics. *ChemRxiv* **2024**, 10.26434/chemrxiv–2024–8kfcb.

(34) Aroeira, G. J.; Kairys, K. T.; Ribeiro, R. F. Coherent transient exciton transport in disordered polaritonic wires. *Nanophotonics* **2024**, *13*, 2553–2564.

(35) Mandal, A.; Taylor, M. A.; Weight, B. M.; Koessler, E. R.; Li, X.; Huo, P. Theoretical advances in polariton chemistry and molecular cavity quantum electrodynamics. *Chemical Reviews* **2023**, *123*, 9786–9879.

(36) Tichauer, R. H.; Feist, J.; Groenhof, G. Multi-scale dynamics simulations of molecular polaritons: The effect of multiple cavity modes on polariton relaxation. *The Journal of Chemical Physics* **2021**, *154*.

(37) Taylor, M.; Mandal, A.; Huo, P. Light-Matter Interaction Hamiltonians in Cavity Quantum Electrodynamics. **2024**,

(38) Qiu, L.; Mandal, A.; Morshed, O.; Meidenbauer, M. T.; Girten, W.; Huo, P.; Vamivakas, A. N.; Krauss, T. D. Molecular polaritons generated from strong coupling between CdSe nanoplatelets and a dielectric optical cavity. *The Journal of Physical Chemistry Letters* **2021**, *12*, 5030–5038.

(39) Taylor, M. A.; Weight, B. M.; Huo, P. Reciprocal asymptotically decoupled Hamiltonian for cavity quantum electrodynamics. *Physical Review B* **2024**, *109*, 104305.

(40) Ying, W.; Mondal, M. E.; Huo, P. Theory and quantum dynamics simulations of exciton-polariton motional narrowing. *The Journal of Chemical Physics* **2024**, *161*.

(41) Lai, Y.; Ying, W.; Huo, P. Non-Equilibrium Rate Theory for Polariton Relaxation Dynamics. **2024**,

(42) Klafter, J.; Sokolov, I. M. *First steps in random walks: from tools to applications*; OUP Oxford, 2011.

(43) Delor, M.; Weaver, H. L.; Yu, Q.; Ginsberg, N. S. Imaging material functionality through three-dimensional nanoscale tracking of energy flow. *Nature materials* **2020**, *19*, 56–62.

(44) Basov, D.; Fogler, M.; García de Abajo, F. Polaritons in van der Waals materials. *Science* **2016**, *354*, aag1992.